photochem

MDPI

Article

Can Implicit Solvation Methods Capture Temperature Effects on the Infrared Features of Astrophysical Ices?

Daniel A. B. Oliveira [1,*], Víctor S. A. Bonfim [2,3,4], Felipe Fantuzzi [4,*] and Sergio Pilling [5,*]

[1] Departamento de Ciências Naturais, Universidade Federal do Norte do Tocantins, Araguaína 77824-838, TO, Brazil
[2] Instituto de Física, Universidade de Brasília, Brasilia 70919-970, DF, Brazil; v.bonfim@kent.ac.uk
[3] Centro Internacional de Física, Universidade de Brasília, Brasília 70910-900, DF, Brazil
[4] Chemistry and Forensic Science, School of Natural Sciences, University of Kent, Park Wood Rd., Canterbury CT2 7NH, UK
[5] Instituto de Pesquisa e Desenvolvimento, Universidade do Vale do Paraíba, São José dos Campos 12244-000, SP, Brazil
* Correspondence: danielchem@uft.edu.br (D.A.B.O.); f.fantuzzi@kent.ac.uk (F.F.); spilling@univap.br (S.P.)

Abstract: Astrophysical ices play a crucial role in the chemistry of cold interstellar environments. However, their diverse compositions, temperatures, and grain morphologies pose significant challenges for molecular identification and quantification through infrared observations. We investigate the ability of implicit solvation approaches to capture temperature-dependent infrared spectral features of CO_2 molecules embedded in astrophysical ice analogues, comparing their performance to that of explicit ice models and experimental data. Using DFT calculations and vibrational frequency scaling, we model CO_2 trapped in both amorphous (cold) and crystalline (warm) H_2O ice clusters. The implicit model qualitatively identifies certain trends but fails to reliably capture the magnitude of frequency shifts and band strengths. Explicit models correctly reproduce the gas-to-solid redshifts for both the asymmetric stretch and bending modes; however, neither approach successfully replicates the experimentally observed temperature-dependent trend in the bending mode. While continuum-like methods may be useful as first-order approximations, explicit modelling of the molecular environment is essential for accurately simulating the infrared spectral behaviour of CO_2 in astrophysical ices and for interpreting observational data on ice composition and evolution.

Keywords: astrochemistry; astrophysical ices; density functional theory; infrared spectroscopy

Received: 18 December 2024
Revised: 9 February 2025
Accepted: 12 February 2025
Published: 14 February 2025

Citation: Oliveira, D.A.B.; Bonfim, V.S.A.; Fantuzzi, F.; Pilling, S. Can Implicit Solvation Methods Capture Temperature Effects on the Infrared Features of Astrophysical Ices? *Photochem* **2025**, *5*, 5. https://doi.org/10.3390/photochem5010005

1. Introduction

Inside cold astrophysical environments, such as dense molecular clouds, the midplane of protoplanetary discs, the obscured regions of young stellar objects (YSOs), comets, and the frozen surfaces of small Solar System bodies, a variety of molecules can be found within solid matrices. These ice mantles, often rich in water, incorporate a diverse array of molecular species, including CO [1,2], CO_2 [3,4], CH_4 [5,6], HCN [7,8], NH_3 [9,10], SO_2 [11,12], HCOOH [13], and CH_3OH [14,15], among others [16–29]. The physical and chemical conditions of these ice-bearing regions vary substantially, leading to broad differences in the ice morphology, porosity, composition, and temperature. Such variability imposes significant challenges for the identification and quantification of molecular abundances through infrared (IR) observations. IR spectra carry the signature of both the molecular species and their local environment, yet interpreting these spectra requires detailed knowledge of how the physical and chemical characteristics of the ice influence vibrational features [30].

The recent advent of the James Webb Space Telescope (JWST) brings unprecedented sensitivity and spectral resolution to the study of molecular ices in various astrophysical environments. Indeed, the JWST's near- and mid-infrared instruments provide detailed absorption profiles that can reveal subtle signatures of temperature, composition, and microstructure in interstellar ices [31]. Its capabilities enable the detection and characterisation of key ice components even in distant and obscured regions, offering new opportunities to test theoretical models and laboratory data against observations. In this context, refining our understanding of how the local environment shapes IR spectral features becomes crucial for interpreting JWST data and utilising its full scientific potential.

Among the molecules trapped in astrophysical ices, CO_2 has been extensively studied, with abundant laboratory and observational data available over a wide temperature range. For example, Collings et al. (2004) [32] reported that the desorption temperature of pure CO_2 in an astrophysical ice environment typically lies between 70 and 80 K. However, when CO_2 is embedded within water-dominated ice mixtures, it can remain trapped until temperatures near 160 K, when water itself begins to desorb [33]. This extended retention arises from a complex interplay of factors. Some CO_2 molecules desorb readily once heated, while others remain confined in micropores or weakly but persistently interact with water molecules through hydrogen bonding analogues, van der Waals forces, or dipole–dipole interactions. These interactions are sufficiently strong to prevent desorption, causing the CO_2 molecules to remain bound to the water matrix until temperatures reach the desorption threshold of water. Furthermore, such local interactions significantly affect not only desorption behaviour but also the IR spectral signatures of the embedded species.

Molecular abundances in cold astrophysical environments are often derived from IR absorption band areas linked to specific vibrational modes [17,34,35]. This approach relies on accurately known band strengths (A), which correlate the observed spectral features with the underlying molecular column densities [35–38]. However, band strengths are not universal constants; they depend on the molecular environment and can vary with ice composition, density, and temperature. Thus, relying exclusively on literature values obtained under controlled conditions—often for pure ices or idealised binary mixtures—may introduce uncertainties when extrapolating to actual, heterogeneous astrophysical conditions. Addressing these discrepancies demands a better understanding of how environmental factors modulate vibrational features and band strengths [36,38,39].

Recent theoretical and experimental studies underscore the complexity of these influences. The dielectric environment of the ice, often parameterised by its dielectric constant (ε), affects both frequency shifts and band intensities. A prior theoretical investigation [40] demonstrated that increasing ε generally enhances IR band intensities while producing opposite trends in frequency shifts. Such behaviour reflects the delicate balance between the local electric field, molecular orientation, hydrogen bonding patterns, and the matrix structure. Similarly, laboratory experiments have shown that temperature and chemical composition produce measurable changes in IR band positions and strengths [41–43]. These variations highlight the importance of capturing the subtleties of the molecular environment, including temperature-dependent ordering and pore collapse, the formation or destruction of hydrogen-bonding networks, and the extent of molecular segregation within the ice matrix. Accurately interpreting spectroscopic data has become even more critical with the exceptional capabilities of JWST.

To tackle these complexities, computational modelling has emerged as a powerful tool. Two approaches dominate: (i) implicit models, which represent the surrounding environment as a dielectric continuum characterised by a bulk property (ε); and (ii) explicit models, which incorporate discrete solvent (or "host" ice) molecules to directly capture local interactions. Implicit models offer computational efficiency and can provide first-order estimates

of environmental effects, making them appealing when dealing with large systems or when detailed structural information is unavailable. However, their continuum nature may fail to reproduce subtle local interactions essential for interpreting fine temperature-dependent changes. Explicit models, on the other hand, are more computationally demanding but can accurately capture hydrogen bonding, dipole–dipole interactions, local orientational disorder, and confinement effects within amorphous and crystalline ice matrices.

Previously, the role of temperature on IR spectral features was examined using implicit solvent models only [44]. While these studies explored the influence of a polar medium, they could not account for the specific local arrangements and discrete interactions captured by explicit modelling. The present work extends beyond these initial efforts by benchmarking implicit and explicit approaches against experimental data for CO_2 embedded in cold (amorphous) and warm (crystalline) H_2O ice clusters. Through the exploration of both frequency shifts and band strengths of the CO_2 asymmetric stretch (as) and bending (δ) modes, this study aims to determine whether implicit solvation methods can adequately reproduce the nuanced temperature-dependent spectral trends observed experimentally. Ultimately, we seek to clarify under which conditions implicit models remain useful approximations and when explicit treatments are necessary for accurate astrophysical interpretations. This is especially relevant for interpreting upcoming JWST measurements and advancing our understanding of the physicochemical processes governing astrophysical ices.

In the sections that follow, we outline our computational methods (both implicit and explicit), present a detailed analysis of the structural and vibrational characteristics of CO_2-bearing ices under varying conditions, and compare these results to laboratory data. Through this comprehensive evaluation, we aim to advance our understanding of the limitations and strengths of implicit solvation and establish guidelines for more reliable modelling of temperature-dependent IR features in astrophysical ices.

2. Computational Methods

To evaluate the spectral features of CO_2 molecules embedded in water ice matrices, we employed two computational approaches to simulate the influence of the bulk environment: implicit and explicit solvation models, each capturing distinct aspects of the molecular surroundings.

The implicit solvation approach uses the polarised continuum model (PCM) [45,46] in its integral equation formalism [47] to represent the average electric field generated by the surrounding water molecules in the ice. This method parameterises the environment through the ε value of the ice, which varies depending on its temperature. The warm ice (labelled as **iw**) was assigned a higher ε value of 180.0, while the cold ice (labelled as **ic**) was described using a lower ε value of 3.0. This approach has been widely applied to simulate the influence of the surrounding icy matrix on molecular reactivity and IR features [40,44,48–52]. While PCM was originally developed for liquid-phase systems and may not rigorously model solid-phase interactions, it serves as a practical first approximation to analyse the stabilising effects of a dielectric medium on vibrational properties [51]. In interstellar ice models, temperature variations affect the cavity's dielectric environment, influencing how the icy matrix stabilises embedded molecules and alters their vibrational features.

The explicit solvation approach, in contrast, captures the discrete interactions between individual water molecules and CO_2. To model these effects in the cold, amorphous ice environment, we adopted a modified protocol based on the method developed by Woon (2024) [53]. Specifically, a three-dimensional amorphous cluster of 95 water molecules, obtained from ErgoSCF [54] and previously optimised, was used as a representative finite system. This cluster effectively simulates the irregular, hydrogen-bonded network characteristic of amorphous water ice.

Seven molecular conformations, labelled as ***cn*** (***n*** from 1 to 7), were generated by embedding a CO_2 molecule at different positions within the cluster, each with a random orientation relative to the surrounding water molecules. To preserve the structural integrity of the ice and to focus on the interactions between the CO_2 molecule and its local environment, the water cluster was initially kept frozen during the density functional theory (DFT) optimisation of CO_2. Subsequently, all water molecules within 3.0 Å of CO_2 were allowed to fully relax. This approach was adopted based on high-level ab initio studies indicating that H_2O–CO_2 interactions can be comparable in strength to H_2O–H_2O hydrogen bonding [55]. The 3.0 Å cutoff was chosen as it encompasses the primary H_2O–CO_2 interactions, which predominantly occur within this range [56]. As such, these interactions may induce local rearrangements in the surrounding ice lattice. While this method does not rigorously identify the global minimum of the system, it offers a more realistic representation of interstellar conditions, where H_2O layers preferentially form on dust grains before CO_2 is later adsorbed or incorporated into a pre-existing ice layer [24,25], inducing only local structural modifications.

Vibrational frequencies and band strengths of CO_2 were calculated for each conformation, with the final values obtained by averaging the results across the distinct conformations. Freezing the water molecules beyond the immediate vicinity of CO_2 ensures computational efficiency while preserving the amorphous nature of the ice structure. Averaging over multiple CO_2 conformations, each interacting with different local environments, effectively accounts for structural heterogeneities and a variety of interaction sites, thereby mitigating any potential bias from using a single configuration. Additionally, the vibrational frequencies and intensities were averaged across all conformations regardless of their individual energies, reflecting the non-equilibrium nature of the amorphous ice system. This approach smooths out peculiarities of any specific configuration, yielding results that are more representative of the vibrational spectrum of the amorphous ice as a whole.

In turn, the crystalline, warm water ice was simulated using a cluster model containing 64 water molecules and derived from the cubic ice phase (**Ic**), a metastable crystalline form of ice [57,58]. Unlike the more stable hexagonal ice (**Ih**), which predominates under standard atmospheric conditions, **Ic** features a proton-disordered lattice with water molecules arranged tetrahedrally, each participating in four hydrogen bonds (two as donors and two as acceptors) [59,60]. This cubic structure serves as an idealised representation of warm, crystalline astrophysical ice. To model the system, seven conformations, labelled as **w*n*** (***n*** from 1 to 7), were generated with CO_2 molecules trapped in different optimised positions within a previously optimised **Ic** cluster. Vibrational frequencies and band strengths were calculated for each configuration using the same methodology as the amorphous, cold ice model; thus, the final values were obtained by averaging the results across all conformations.

For both implicit and explicit models, vibrational scaling factors were applied to account for anharmonicities. Different scaling factors were used for the asymmetric stretch and bending modes, the two modes of primary interest in this study. These values were determined by calibrating the computed frequency values of isolated CO_2 against experimental gas-phase data [61]. In the case of the ice models, the two CO_2 bending modes are not degenerate, reflecting the influence of the ice environment. To address this, the bending mode frequency was calculated as the average of the two individual bending mode frequencies, while the band strength was taken as the sum of the two.

All calculations were performed using DFT with the ωB97X-D functional [62] and the 6-31+G(d) basis set [63–66]. These were carried out using the Gaussian 16 package, Revision C.01 [67]. To evaluate the suitability of our computational approach, full optimisations and vibrational frequency analyses were conducted on two $CO_2(H_2O)_n$ clusters taken from Ramachandran and Ruckenstein (2011) [68], employing the same functional with basis sets

up to 6-311+G(d,p). For more details, see the Supplementary Information (SI) file. The results indicate that both geometries and vibrational frequencies exhibit minimal sensitivity to basis set expansion and remain consistent with those obtained at the MP2/aug-cc-pVDZ level of theory reported by the original authors. The 3D images of the optimised clusters used for the cold and warm ice models are shown in Figures 1 and 2, respectively.

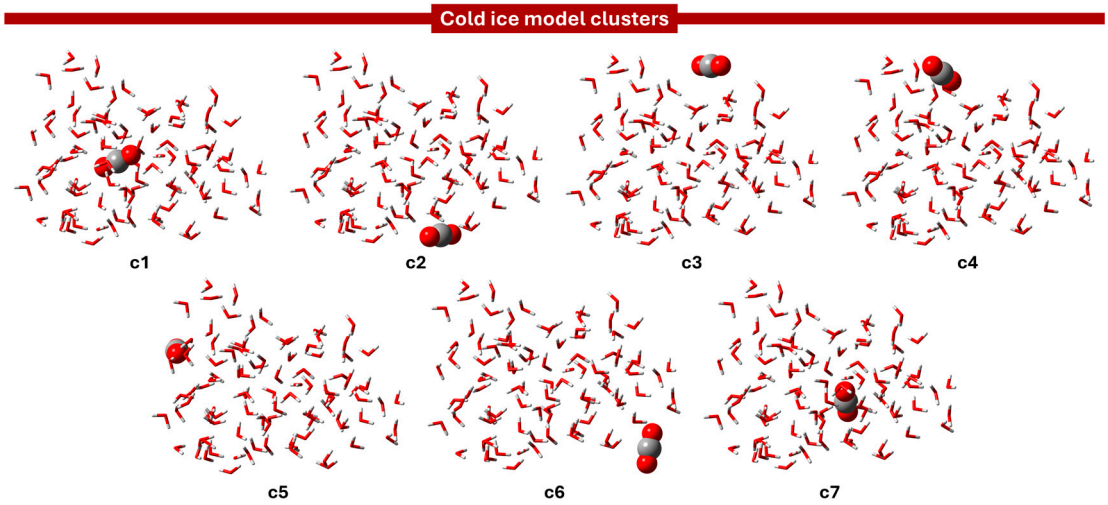

Figure 1. Models of cold ice with CO_2 molecules in various positions throughout the structure. Partially constrained geometry optimisations were carried out at the ωB97X-D/6-31+G(d) level of theory.

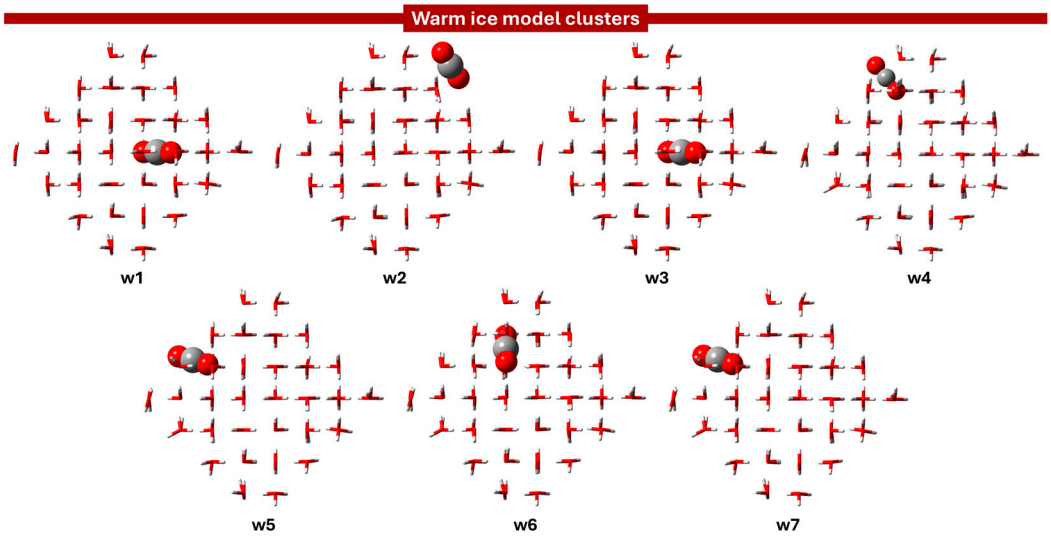

Figure 2. Models of warm ice with CO_2 molecules in various positions throughout the structure. Partially constrained geometry optimisations were carried out at the ωB97X-D/6-31+G(d) level of theory.

3. Results and Discussion

The results are organised as follows. Section 3.1 examines the structural properties of the ice-model CO_2/H_2O clusters generated using the explicit approach. Section 3.2 compares the vibrational frequencies of CO_2 derived from both explicit and implicit models. Finally, Section 3.3 evaluates the CO_2 band strengths predicted by these methods. The astrophysical implications of the findings are discussed throughout.

3.1. Structural Properties of the Ice-Model CO_2/H_2O Clusters

The computed properties of CO_2 molecules embedded within both explicit and implicit ice models are summarised in Table 1, including the electronic energies of each individual cluster/model configuration and their corresponding infrared features. These data provide a comprehensive overview of how local structural motifs and the surrounding dielectric environment influence the vibrational characteristics of CO_2 in water ice matrices.

Table 1. Summary of the energetic and spectroscopic properties (as: asymmetric stretch; δ: bending) of CO_2 in various environments, including gas phase, explicit ice models (cold and warm), and implicit models. All calculations were performed at the ωB97X-D/6-31+G(d) level of theory. Experimental data from Sandford and Allamandola (1990) [61] are included for comparison, with a focus on the asymmetric stretch and bending vibrational modes. The relative electronic energies of the distinct ice clusters of the explicit model are presented in kcal mol^{-1}, with values provided in parentheses in the second column.

Structure	Energy a.u. (kcal mol^{-1})	Frequency (as) cm^{-1}	Strength (as) arb. Units	Frequency (δ) cm^{-1}	Strength (δ) arb. Units
gas phase					
CO_2 (calcd)	−188.526940	2455.9	715.69	663.3	72.32
CO_2 (exp) †	-	2348.0	-	667.7	-
scaling factor	-	0.9561	-	1.0066	-
cold ice (explicit model)					
c1	−7448.216883 (0.0)	2338.7	750.23	618.4	188.37
c2	−7448.202834 (8.8)	2345.9	721.31	659.7	102.11
c3	−7448.201316 (9.8)	2345.9	642.29	659.0	98.47
c4	−7448.201026 (10.0)	2345.9	654.71	664.8	79.46
c5	−7448.203651 (8.3)	2347.8	716.81	658.8	94.03
c6	−7448.200589 (10.2)	2348.6	736.73	664.4	81.79
c7	−7448.208324 (5.4)	2339.7	569.41	651.5	111.40
average	-	2344.6	684.50	653.8	107.95
warm ice (explicit model)					
w1	−5079.200727 (20.8)	2343.4	548.85	650.1	160.00
w2	−5079.233846 (0.0)	2345.2	702.54	656.9	104.98
w3	−5079.200839 (20.7)	2343.6	551.42	651.3	160.12
w4	−5079.227835 (3.8)	2351.1	798.32	657.7	113.02
w5	−5079.207617 (16.5)	2336.7	634.71	651.3	153.36
w6	−5079.192575 (25.9)	2344.4	505.67	652.9	168.48
w7	−5079.207590 (16.5)	2336.6	634.53	651.2	153.45
average	-	2343.0	625.15	653.1	144.77
implicit model					
ic (ε = 3.0)	−188.528601	2327.5	937.12	663.9	84.61
iw (ε = 180.0)	−188.529923	2311.5	1132.96	661.9	95.20
experimental data †					
ec (10 K)	-	2341.5	1.00	653.4	1.00
ew (150 K)	-	2339.3	0.93	654.2	1.07

† Taken from Sandford and Allamandola (1990) [61].

For the explicit cold ice clusters (denoted **c1**–**c7**), each comprising a CO_2 molecule interacting with a finite amorphous assembly of 95 H_2O molecules, the calculated electronic energies range from −7448.216883 (**c1**) to −7448.200589 (**c6**) hartree. While some clusters feature CO_2 embedded within the ice matrix, others, such as **c6**, have the CO_2 molecule interacting at the cluster edges. The resulting energy difference spans approximately 10.2 kcal mol^{-1}, indicating that subtle variations in the local coordination environment—including hydrogen-bonding patterns, hydrogen-bond distances, and molecular orientations—can significantly influence cluster stabilisation. In particular, the structural differences between **c1**

and **c7**—the latter being a higher-energy cluster with a partially confined CO_2—underscore the crucial role of hydrogen-bond-type interactions in stabilising CO_2 within the ice matrix.

To clarify these interactions more concretely, Figure 3 compares the local environments around the CO_2 molecule in **c1** and **c7**. In the **c1** configuration, three H···O(CO_2) and three O···C(CO_2) interactions contribute to its stability. Regarding the hydrogen bonds, one of these interactions involves a single H···O(CO_2) contact with a bent geometry (COH angle: 151.6°) and an H···O distance of 1.977 Å. The remaining two hydrogen bond interactions involve the same oxygen atom from CO_2, with COH angles of 121.3° and 123.4°, and H···O distances of 2.094 Å and 2.007 Å, respectively. Additionally, the three O···C(CO_2) interactions occur at 2.482 Å, 2.611 Å and 2.681 Å, resembling the T-shaped structure that represents the global minimum of the H_2O–CO_2 pair [55]. These combined interactions play a crucial role in stabilising the cluster, explaining why **c1** is the most stable among the cold clusters.

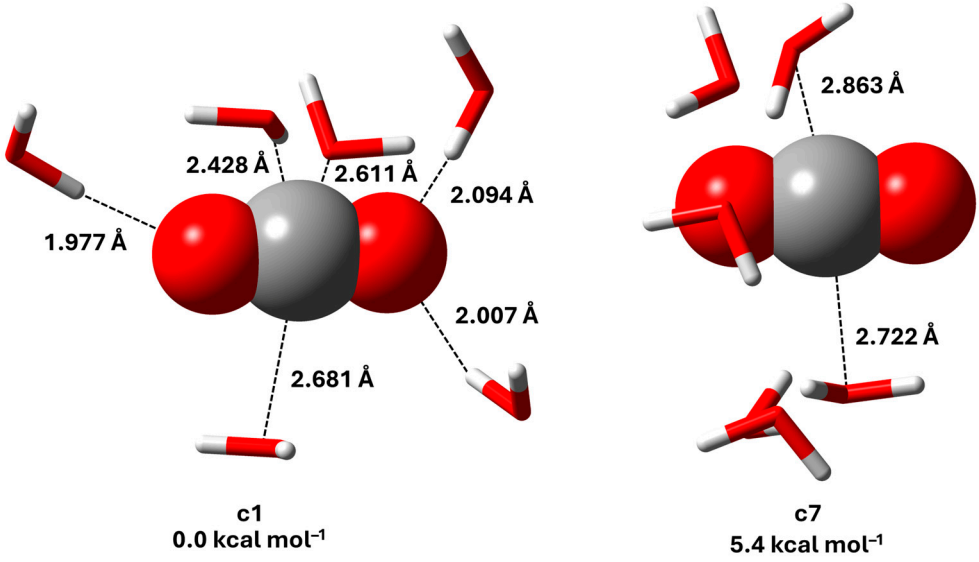

Figure 3. Comparison of the local environments around the CO_2 molecule in the explicit cold ice clusters **c1** (**left**) and **c7** (**right**). The **c1** configuration features three notable H···O(CO_2) interactions, with contact distances of 1.977 Å, 2.007 Å and 2.094 Å, while the **c7** configuration lacks such interactions. Partially constrained geometry optimisations were performed at the ωB97X-D/6-31+G(d) level of theory.

In contrast, the **c7** configuration lacks direct H···O(CO_2) contacts and contains only two O···C(CO_2) interactions, at 2.722 Å and 2.863 Å, illustrating how the absence of additional stabilising interactions correlates with its higher energy. Collectively, these findings suggest that amorphous pockets where favourable H···O(CO_2) and O···C(CO_2) interactions can form act as preferential sites for CO_2 accommodation, reducing the overall energy and making these configurations thermodynamically more favourable.

Turning to the warm ice clusters (denoted **w1**–**w7**, containing 64 water molecules), which represent a more crystalline and ordered ice environment, we observe an even greater variation in energy range compared to the cold ice model clusters. The most stable configuration, **w2**, exhibits an electronic energy of −5079.233846 hartree, while the least stable configuration, **w6**, has an energy of −5079.192575 hartree. This corresponds to an energy difference of about 25.9 kcal mol^{-1} across the **w**-series. In the most stable **w2** arrangement, the CO_2 molecule resides at the cluster's periphery. Such a position effectively mimics a surface-like environment where the CO_2 is adsorbed onto, rather than fully enclosed by, the ice structure.

This comparison between the cold amorphous (**c**-series) and warm (**w**-series) clusters is instructive. In the amorphous environment, configurations that allow CO_2 to form local

H···O contacts are energetically favoured, suggesting that embedded pockets where such interactions prevail are likely to trap CO_2 molecules. In contrast, the warm ice models, more structured and closer to crystalline order, seem to favour configurations that retain the integrity of the ice lattice. Here, placing CO_2 on the surface minimises disruption to the underlying lattice, even if fewer direct H···O(CO_2) interactions exist. Therefore, while the amorphous structure thermodynamically favours the incorporation of CO_2 into suitable cavities with stabilising contacts, the more ordered system tends to preserve its crystalline network by stabilising CO_2 at the interface, rather than fully integrating it into the ice interior.

Finally, it is worth noting that **w5** and **w7** optimised to virtually identical structures, with the CO_2 molecule positioned near the edge of the clusters. Their respective energies are −5079.207617 and −5079.207590 hartree, respectively. Despite their similarity, both structures were retained in the analysis to maintain consistency in the number of clusters evaluated across the warm ice models. Furthermore, as these structures were initially generated with distinct, randomly oriented starting configurations, their inclusion ensures that the sampling adequately represents the diversity of possible local environments within the crystalline ice framework.

3.2. CO_2 Vibrational Frequencies: Implicit Versus Explicit Solvation

We now shift our focus to the comparison of vibrational frequency trends obtained using implicit and explicit solvation models. Whenever appropriate, these results are compared to the experimental data of Sandford and Allamandola (1990) [61], who measured CO_2/H_2O ices with a 1:20 ratio at temperatures of 10 K (herein referred to as **ec**) and 150 K (**ew**). This dataset was chosen due to its systematic investigation of temperature-dependent spectral changes, providing a well-defined baseline for evaluating the performance of the computational models. Our primary interest lies in the CO_2 asymmetric stretch (as) and bending (δ) vibrational modes.

Before discussing the comparison, it is important to observe that the computed frequencies were initially scaled using mode-specific scaling factors. Through a comparison between gas-phase computational results at the ωB97X-D/6-31+G(d) level of theory to experimental gas-phase frequencies, we derived scaling factors of 0.9561 for the asymmetric stretch and 1.0066 for the bending mode. For reference, the gas-phase calculation yielded scaled values of 2348.0 cm^{-1} for the asymmetric stretch and 667.7 cm^{-1} for the bending mode (see Table 1).

We start by discussing the asymmetric stretch mode. For the explicit cold ice clusters (**c1**–**c7**), the scaled asymmetric stretch frequencies range from 2338.7 cm^{-1} (**c1**) to 2348.6 cm^{-1} (**c6**). These extremes correspond to deviations from the gas-phase frequency of –9.3 cm^{-1} (negative sign, indicating a redshift) and +0.6 cm^{-1} (positive sign, indicating a blueshift), respectively. The average value across the cold ice clusters is 2344.6 cm^{-1}, which is slightly redshifted by –3.4 cm^{-1} compared to the gas-phase reference. Notably, the **c1** cluster, featuring strong H···O(CO_2) interactions, shows a more pronounced redshift, suggesting that CO_2 stabilised within water-rich pockets forms stronger interactions and therefore undergoes more significant frequency reductions. Experimental data for the cold ice (**ec**) report an asymmetric stretch band at 2341.5 cm^{-1}, representing a –6.5 cm^{-1} redshift. The explicit model's prediction (–3.4 cm^{-1}) is reasonably close to this experimental value, differing by 3.1 cm^{-1}.

For the explicit warm ice clusters (**w1**–**w7**), the scaled asymmetric stretch frequencies vary from 2336.6 cm^{-1} (**w7**) to 2351.1 cm^{-1} (**w4**), corresponding to deviations of −11.4 cm^{-1} to +3.1 cm^{-1} relative to the gas-phase value. The average value for the warm ice clusters is 2343.0 cm^{-1}, a –5.0 cm^{-1} redshift from the gas phase. Experimentally, the warm ice (**ew**)

frequency is 2339.3 cm^{-1}, indicating a –8.7 cm^{-1} redshift. Although the explicit model shows a smaller redshift than the experiment, it correctly predicts the trend that the warm ice is more redshifted than the cold ice.

From these comparisons, several observations emerge. Experimentally, the warm ice is redshifted by an additional –2.2 cm^{-1} compared to the cold ice. The explicit model reproduces this trend but with a smaller difference (-1.6 cm^{-1}). Given that the experimental differences are quite subtle, the fact that the explicit simulations capture the correct qualitative behaviour is noteworthy (see Figure 4). Moreover, the strong redshifts predicted by the explicit model for certain cold ice clusters suggest that if the ice were to consist predominantly of pockets stabilising CO_2 molecules through H···O(CO_2) interactions, one would expect substantial redshifts to occur. The relatively modest experimental redshifts, however, imply that under the experimental conditions, CO_2 does not predominantly reside in such stabilising environments. Instead, it likely remains at or near the surface or in larger pores and voids lacking strong H···O(CO_2) interactions. These findings are consistent with recent discussions by Schiltz et al. (2024) [69] on the nature of CO_2/H_2O ice mixtures in planetary environments like Ganymede and Europa.

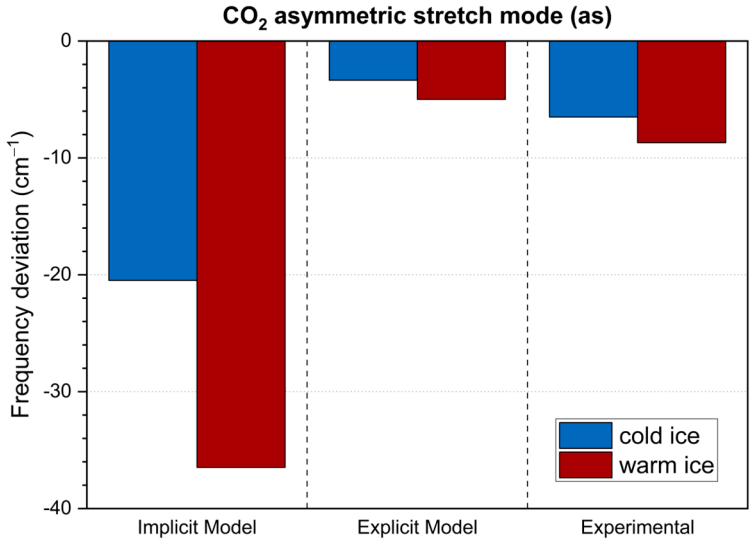

Figure 4. Frequency deviations of the CO_2 asymmetric stretch mode relative to the gas-phase value (2348.0 cm^{-1}) for different ice types. Results are shown for experimental data, taken from Sandford and Allamandola (1990) [61], as well as implicit and explicit models for cold and warm ice.

Turning to the implicit model, we see a markedly different pattern. The implicit cold ice model (**ic**, $\varepsilon = 3.0$) predicts a scaled asymmetric stretch at 2327.5 cm^{-1}, representing a -20.5 cm^{-1} redshift. The implicit warm ice model (**iw**, $\varepsilon = 180.0$) places the asymmetric stretch at 2311.5 cm^{-1}, yielding a -36.5 cm^{-1} redshift. While both implicit models qualitatively reproduce the trend that the warm ice is more redshifted than the cold ice, the magnitude of these shifts is greatly overestimated compared to the experiment and the explicit model. Experimentally, the cold-to-warm redshift difference is only -2.2 cm^{-1}, while the explicit model yields -1.6 cm^{-1}; in contrast, the implicit model predicts a much larger shift of -16.5 cm^{-1}.

This overestimation is not unexpected. As shown by Pilling and Bonfim (2020) [40], higher ε values in the PCM framework lead to increased redshifts. Although substituting the DFT approach with wavefunction-based methods like MP2 can reduce these deviations [40], the implicit model still tends to overpredict redshifts relative to both the experiment and the explicit model. Nonetheless, the implicit approach does correctly iden-

tify the qualitative trend that higher ε (associated with a warmer, more polar environment) leads to greater redshifts in vibrational frequencies.

Next, we focus on the CO_2 bending mode. From Table 1, it can be seen that the explicit cold ice clusters (**c1**–**c7**) yield CO_2 bending frequencies ranging from 618.4 cm^{-1} (**c1**, a redshift deviation of −49.3 cm^{-1}) to 664.4 cm^{-1} (**c6**, a redshift deviation of −3.3 cm^{-1}), with an average value of 653.8 cm^{-1}. As before, a larger redshift deviation correlates with CO_2 molecules occupying denser pockets featuring H···O(CO_2) interactions. On average, the explicit model predicts a −13.9 cm^{-1} redshift. Notably, the experimental cold ice (**ec**) bending mode is observed at 653.4 cm^{-1}, representing a mere –0.4 cm^{-1} difference from the explicit model's average and a −14.3 cm^{-1} redshift from the gas-phase reference. Thus, the explicit model closely replicates the observed redshift for the cold ice bending mode.

For the warm ice clusters (**w1**–**w7**), the CO_2 bending frequencies range from 650.1 cm^{-1} (**w1**, −17.6 cm^{-1} redshift) to 657.7 cm^{-1} (**w4**, −10.0 cm^{-1} redshift), with an average of 653.1 cm^{-1}, corresponding to a −14.6 cm^{-1} redshift. Experimentally, the warm ice (**ew**) bending mode is at 654.2 cm^{-1}, only 1.1 cm^{-1} higher than the explicit model's average, and −13.5 cm^{-1} relative to the gas phase. These results demonstrate that the model accurately captures both the absolute bending mode frequencies and the redshift magnitudes within a remarkably small deviation from the experiment. However, while both the experimental and computational results for the CO_2 asymmetric stretch exhibited increasing redshifts from cold to warm ice (explicit model: −1.6 cm^{-1}; experiment: −2.2 cm^{-1}), the computationally derived bending mode using the explicit model fails to reproduce the experimentally anticipated opposite trend with increasing temperature (explicit model: −0.7 cm^{-1}; experiment: +0.8 cm^{-1}). This discrepancy, though subtle, likely arises from the greater sensitivity of bending modes to local perturbations within the ice lattice. Given their lower vibrational frequencies, bending modes are inherently more susceptible to anharmonic effects and long-range structural influences, which may not be fully accounted for in the current model. Nevertheless, the overall agreement remains strong, reinforcing the model's ability to describe CO_2 vibrational behaviour in different ice environments with high fidelity (see Figure 5).

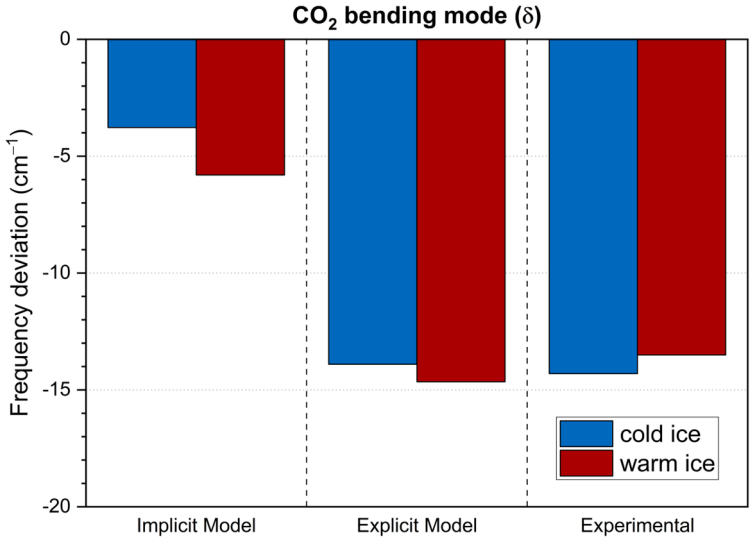

Figure 5. Frequency deviations of the CO_2 bending mode relative to the gas-phase value (667.7 cm^{-1}) for different ice types. Results are shown for experimental data, taken from Sandford and Allamandola (1990) [61], as well as implicit and explicit models for cold and warm ice.

Turning to the implicit model, the CO_2 bending mode of the cold ice (**ic**) is computed at 663.9 cm^{-1}, corresponding to a −3.8 cm^{-1} redshift and 10.5 cm^{-1} less than that ob-

served experimentally. For the warm ice (**iw**), the bending mode appears at 661.9 cm^{-1}, a -5.8 cm^{-1} redshift and 7.7 cm^{-1} less than the experimental value. The implicit model, therefore, predicts a slightly larger redshift from cold to warm than that of the explicit model (implicit model: -1.6 cm^{-1}; explicit model: -0.7 cm^{-1}), both being inverted with respect to the experimental trend.

These findings indicate that, while the implicit model provides a reasonable first approximation, it is less accurate than the explicit model in capturing the deviations between the gas and solid phases for both the asymmetric and bending modes. Additionally, it fails to reproduce the subtle temperature-dependent shifts observed in the lower-frequency CO_2 bending mode. However, the discrepancies between the experimental and computational trends remain relatively small, with deviations of only 1.5 cm^{-1} for the explicit model and 2.4 cm^{-1} for the implicit model.

3.3. CO_2 Band Strengths: Implicit Versus Explicit Solvation

In this section, we turn our attention to the CO_2 band strengths within the studied ice matrices. As discussed by Dartois and D'Hendecourt [70], the band strength of a vibrational transition is a key physicochemical parameter that connects the quantity of a given molecular species to its interaction with incoming electromagnetic radiation at a particular frequency (or wavenumber). The integrated band strength, A (in cm $molecule^{-1}$) can be expressed as follows:

$$A = \frac{m}{\rho N_A} \int 4\pi \, k\nu d\nu \tag{1}$$

where k is the imaginary part of the complex index of refraction, ν is the wavenumber, ρ is the density of the material in units of g cm^{-3}, N_A is the Avogadro constant (6.022×10^{23} molecules mol^{-1}), and m is the molecular weight of the considered molecular species, in units of g mol^{-1}. The integral in Equation (1), relates directly to the integrated band area S of a specific infrared transition.

Assuming that the band profile does not change significantly with the concentration of the species in the ice, and noting that the band area S (in cm^{-1}) is proportional to the band intensity (i.e., $S \propto I$), we can relate A and I. Under these simplifying conditions, the integrated band strength can also be expressed as [71–73]:

$$A = \frac{2.3}{N} S \tag{2}$$

where N is the column density (molecules cm^{-2}) of the species. In other words, the band strength is intimately connected to the local abundance of the absorbing species, as well as its interaction with the electromagnetic field.

It is important to keep in mind that band strengths are intrinsic properties of the material and can vary considerably with temperature and morphology, as noted by Maté (2018) [74]. Changes in the physical structure of the ice—such as transitions between amorphous and crystalline phases, compaction, or alterations in porosity—can modify the local dielectric environment. This can, in turn, alter the band strengths and IR features of embedded species. Moreover, when multiple molecular species are mixed within an ice, their mutual interactions can lead to shifts in the band profiles and band strengths relative to those of the pure ices. Such effects are documented extensively in the literature [70–73,75].

For instance, Schmitt et al. (1998) [75] demonstrated that the chemical environment, defined by the types of neighbouring molecules, influences IR band profiles. Similarly, Luna et al. (2018) [76] found that heating amorphous astrophysical ices can lead to micropore collapse, an increase in ice density, and changes in the vibrational band profiles of embedded molecules. The segregation of non-polar or weakly interacting species such as CO_2 and

CH_4 within water-rich matrices, as discussed by Bossa et al. (2012) [77], further highlights how molecular rearrangement affects the observed IR spectral features.

Irradiation by energetic particles (e.g., cosmic rays) and subsequent compaction processes can also influence band strengths, as shown in previous studies [78–81]. Likewise, amorphisation of crystalline ices or the presence of contaminants can modify the local dielectric environment and, consequently, the observed IR profiles [78,79,82]. Experimental investigations by Bouwman et al. (2007) [83] and Öberg et al. (2011) [24] illustrate how band strengths of H_2O, CO_2, and other species depend on their intermolecular interactions.

Given the complexity of these factors, understanding the influence of explicit and implicit solvation on band strengths provides key information into how computational models replicate, predict, or diverge from experimentally observed trends. Below, we compare the band strengths predicted by implicit and explicit approaches, examining their capacity to capture the subtle effects of local environments, molecular interactions, and temperature-dependent morphological changes in CO_2-bearing astrophysical ice analogues.

Figure 6 shows the ratio of warm ice to cold ice band strengths for the CO_2 asymmetric stretch and bending modes as predicted by the implicit and explicit models. For comparison, we also include experimental data from Sandford and Allamandola (1990) [61], who reported that the asymmetric stretch band strength decreases by about 0.5% per 10 K increase in temperature, while the bending mode band strength increases by about the same amount.

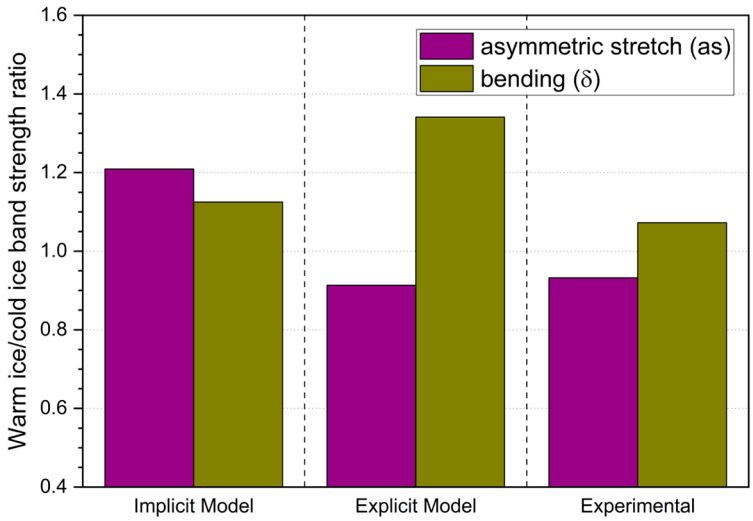

Figure 6. Band strength ratios (warm ice/cold ice) for the CO_2 asymmetric stretch and bending modes in the studied ices, calculated using explicit and implicit models. Experimental data, taken from Sandford and Allamandola (1990) [61], are included for comparison, highlighting the temperature-dependent trends in band strength changes for both vibrational modes.

Focusing first on the asymmetric stretch mode, the explicit model yields band strengths for the cold ice (**c1**–**c7**) ranging from 569.41 (**c7**) to 750.23 (**c1**), with an average of 684.50 (for numerical data, see Table 1). For the warm ice clusters (**w1**–**w7**), the values range from 505.67 (**w6**) to 798.32 (**w4**), averaging 625.15. This leads to a warm/cold ratio of 0.91, which closely matches the experimental ratio of approximately 0.93, both quantitatively and qualitatively.

For the bending mode, the explicit model predicts an average band strength of 107.95 for the cold ice and 144.77 for the warm ice. The resulting ratio of 1.34, though overestimated, remains above 1, aligning reasonably well with the experimental value of 1.07 and confirming that the bending mode band strength increases with temperature. These findings demonstrate that the explicit model successfully captures both the overall trend

and the approximate magnitude of the experimentally observed temperature dependence for both vibrational modes.

Turning to the implicit model, the warm/cold ratio for the bending mode is 95.20/84.61 = 1.13, which is both qualitatively and quantitatively consistent with the experimental findings. However, the implicit model yields a ratio of 1.21 (1132.96/937.12) for the asymmetric stretch mode, in contrast to the observed decrease. While the latter result does not reflect the experimental trend, it is important to note that the implicit model is designed as a first-order approximation. As a continuum-based approach, it does not explicitly account for local interactions at the molecular level. These subtleties, captured by the explicit model, can be crucial for accurately predicting small changes in band strengths associated with temperature variations.

The findings of this study indicate that models explicitly incorporating the surrounding environment molecules are better suited for capturing the intricacies of molecular behaviour in complex settings, particularly in the context of vibrational spectra. For CO_2 embedded in an H_2O matrix, these models accurately reproduce experimental data for both the asymmetric stretch and bending modes, highlighting their ability to predict molecular interactions within interstellar ice matrices and other host-guest systems with high precision. By contrast, the deviations observed in the implicit model highlight its limitations in environments where local host-guest interactions play a crucial role, suggesting that such systems require more nuanced modelling approaches to fully account for these effects.

4. Conclusions

In summary, the present study examined how implicit and explicit approaches perform in modelling the temperature-dependent vibrational features of CO_2 trapped in H_2O ice, with a particular focus on astrophysical conditions. Through a comparison of computational results against experimental data for CO_2-bearing ices at different temperatures, we demonstrated that explicit models, which include individual H_2O molecules and their local interactions, provide a significantly more accurate description of frequency shifts and band strengths than implicit (continuum) models. The explicit approach successfully captures most of the subtle yet critical differences in vibrational behaviour between cold and warm ices, accurately reproducing the measured gas-to-solid redshifts for both the asymmetric stretch and bending modes. It also correctly reflects the contrasting temperature dependencies of the solid-phase redshifts for the asymmetric stretch, with its failure in the bending mode attributable to the mode's minimal temperature dependence (+0.8 cm^{-1} experimentally vs. -0.7 cm^{-1} in the explicit model). In contrast, the implicit model qualitatively identifies the direction of certain trends but fails to reproduce the magnitude of frequency shifts consistently, sometimes overestimating and at other times underestimating them. Moreover, it cannot replicate the intricate interplay of local interactions that govern the observed spectral variations. These findings underscore that while continuum-like methods may be useful as first-order approximations, they cannot reliably account for the intricate molecular-level environments within interstellar ices. Consequently, to interpret observational data and infer molecular abundances or ice properties in astrophysical settings, more nuanced theoretical approaches are needed.

Supplementary Materials: The following supporting information can be downloaded at https://www.mdpi.com/article/10.3390/photochem5010005/s1: Figure S1: Optimised structures of **CW3b** and **CW6a** at the ωB97X-D/6-311+G(d,p) level of theory; Table S1: Summary of the benchmark results for the energetic and spectroscopic properties of the $CO_2(H_2O)_n$ clusters **CW3b** and **CW6a** from Ramachandran & Ruckenstein (2011) [68]. RMSD values include hydrogen atoms. The values in parenthesis in the frequency columns indicate deviations (in cm^{-1}) relative to the ωB97X-D/6-311+G(d,p) reference. Frequency values have been scaled using correction factors derived from the

difference between CO_2 vibrational frequencies computed in the gas phase at each level of theory and the corresponding experimental values. The scaling factors are as follows: as mode: 0.9561 for 6-31+G(d) and 6-31+G(d,p); 0.9517 for 6-311+G(d) and 6-311+G(d,p); δ mode: 1.0066 for 6-31+G(d) and 6-31+G(d,p); 0.9820 for 6-311+G(d) and 6-311+G(d,p); Cartesian coordinates of all structures computed herein.

Author Contributions: Conceptualisation, S.P.; methodology, D.A.B.O., V.S.A.B. and F.F.; formal analysis, D.A.B.O., V.S.A.B. and F.F.; investigation, D.A.B.O., V.S.A.B. and, F.F.; resources, D.A.B.O., F.F. and S.P.; data curation, D.A.B.O., V.S.A.B. and F.F.; writing—original draft preparation, D.A.B.O. and F.F.; writing—review and editing, D.A.B.O., V.S.A.B., F.F. and S.P. All authors have read and agreed to the published version of the manuscript.

Funding: National Institute of Science and Technology on Molecular Sciences (INCT-CiMol), Grant CNPq 406804/2022-2; COST Action CA20129—Multiscale Irradiation and Chemistry Driven Processes and Related Technologies (MultIChem), supported by COST (European Cooperation in Science and Technology). CNPq (projects 302985/2018-2 and 302608/2022-2), FAPESP (projects 2016/22018-7 and 2024/05115-5).

Data Availability Statement: The original contributions presented in the study are included in the article/Supplementary Materials; further inquiries can be directed to the corresponding authors.

Acknowledgments: This article is based upon work from the COST Action CA20129—Multiscale Irradiation and Chemistry Driven Processes and Related Technologies (MultIChem), supported by COST (European Cooperation in Science and Technology). D.A.B.O. appreciates the support from the Universidade Federal do Norte do Tocantins. V.S.A.B. thanks the National Institute of Science and Technology on Molecular Sciences (INCT-CiMol) for a postdoctoral fellowship (Grant No. CNPq 406804/2022-2). F.F. is grateful to the University of Kent for their support. S.P. acknowledges the Brazilian research agencies Conselho Nacional de Desenvolvimento Científico e Tecnológico—CNPq (projects 302985/2018-2 and 302608/2022-2) and Fundação de Amparo à Pesquisa do Estado de São Paulo—FAPESP (projects 2016/22018-7 and 2024/05115-5).

Conflicts of Interest: The authors declare no conflicts of interest.

References

1. Zamirri, L.; Casassa, S.; Rimola, A.; Segado-Centellas, M.; Ceccarelli, C.; Ugliengo, P. IR Spectral Fingerprint of Carbon Monoxide in Interstellar Water–Ice Models. *Mon. Not. R. Astron. Soc.* **2018**, *480*, 1427–1444. [CrossRef]
2. De Barros, A.L.F.; Mejía, C.; Duarte, E.S.; Domaracka, A.; Boduch, P.; Rothard, H.; da Silveira, E.F. Chemical Reactions in H_2O:CO Interstellar Ice Analogues Promoted by Energetic Heavy-Ion Irradiation. *Mon. Not. R. Astron. Soc.* **2022**, *511*, 2491–2504. [CrossRef]
3. Radhakrishnan, S.; Gudipati, M.S.; Sander, W.; Lignell, A. Photochemical Processes in CO_2/H_2O Ice Mixtures with Trapped Pyrene, a Model Polycyclic Aromatic Hydrocarbon. *Astrophys. J.* **2018**, *864*, 151. [CrossRef]
4. Simon, A.; Rajappan, M.; Öberg, K.I. Entrapment of Hypervolatiles in Interstellar and Cometary H_2O and CO_2 Ice Analogs. *Astrophys. J.* **2023**, *955*, 5. [CrossRef]
5. Mejía, C.; de Barros, A.L.F.; Rothard, H.; Boduch, P.; da Silveira, E.F. Radiolysis of Ices by Cosmic-Rays: CH_4 and H_2O Ices Mixtures Irradiated by 40 MeV $^{58}Ni^{11+}$ Ions. *Astrophys. J.* **2020**, *894*, 132. [CrossRef]
6. Mifsud, D.V.; Herczku, P.; Sulik, B.; Juhász, Z.; Vajda, I.; Rajta, I.; Ioppolo, S.; Mason, N.J.; Strazzulla, G.; Kaňuchová, Z. Proton and Electron Irradiations of CH_4:H_2O Mixed Ices. *Atoms* **2023**, *11*, 19. [CrossRef]
7. Gerakines, P.A.; Yarnall, Y.Y.; Hudson, R.L. Direct Measurements of Infrared Intensities of HCN and H_2O + HCN Ices for Laboratory and Observational Astrochemistry. *Mon. Not. R. Astron. Soc.* **2021**, *509*, 3515–3522. [CrossRef]
8. Ozhiganov, M.; Medvedev, M.; Karteyeva, V.; Nakibov, R.; Sapunova, U.; Krushinsky, V.; Stepanova, K.; Tryastsina, A.; Gorkovenko, A.; Fedoseev, G.; et al. Infrared Spectra of Solid HCN Embedded in Various Molecular Environments for Comparison with the Data Obtained with JWST. *Astrophys. J. Lett.* **2024**, *972*, L10. [CrossRef]
9. Escamilla-Roa, E.; Sainz-Díaz, C.I. Amorphous Ammonia–Water Ice Deposited onto Silicate Grain: Effect on Growth of Mantles Ice on Interstellar and Interplanetary Dust. *J. Phys. Chem. C* **2014**, *118*, 3554–3563. [CrossRef]
10. Molpeceres, G.; Tsuge, M.; Furuya, K.; Watanabe, N.; San Andrés, D.; Rivilla, V.M.; Colzi, L.; Aikawa, Y. Carbon Atom Condensation on NH_3–H_2O Ices. An Alternative Pathway to Interstellar Methanimine and Methylamine. *J. Phys. Chem. A* **2024**, *128*, 3874–3889. [CrossRef]

11. Yarnall, Y.Y.; Hudson, R.L. A New Method for Measuring Infrared Band Strengths in H_2O Ices: First Results for OCS, H_2S, and SO_2. *Astrophys. J. Lett.* **2022**, *931*, L4. [CrossRef]
12. Mifsud, D.V.; Herczku, P.; Rahul, K.K.; Ramachandran, R.; Sundararajan, P.; Kovács, S.T.S.; Sulik, B.; Juhász, Z.; Rácz, R.; Biri, S.; et al. A Systematic Mid-Infrared Spectroscopic Study of Thermally Processed SO_2 Ices. *Phys. Chem. Chem. Phys.* **2023**, *25*, 26278–26288. [CrossRef] [PubMed]
13. Chaabouni, H.; Baouche, S.; Diana, S.; Minissale, M. Reactivity of Formic Acid (HCOOH) with H Atoms on Cold Surfaces of Interstellar Interest. *Astron. Astrophys.* **2020**, *636*, A4. [CrossRef]
14. Giuliano, B.M.; Martín-Doménech, R.; Escribano, R.M.; Manzano-Santamaría, J.; Muñoz Caro, G.M. Interstellar Ice Analogs: H_2O Ice Mixtures with CH_3OH and NH_3 in the Far-IR Region. *Astron. Astrophys.* **2016**, *592*, A81. [CrossRef]
15. Müller, B.; Giuliano, B.M.; Goto, M.; Caselli, P. Spectroscopic Measurements of CH_3OH in Layered and Mixed Interstellar Ice Analogues. *Astron. Astrophys.* **2021**, *652*, A126. [CrossRef]
16. Ehrenfreund, P.; Charnley, S.B. Organic Molecules in the Interstellar Medium, Comets, and Meteorites: A Voyage from Dark Clouds to the Early Earth. *Annu. Rev. Astron. Astrophys.* **2000**, *38*, 427–483. [CrossRef]
17. Gibb, E.L.; Whittet, D.C.B.; Chiar, J.E. Searching for Ammonia in Grain Mantles toward Massive Young Stellar Objects. *Astrophys. J.* **2001**, *558*, 702–716. [CrossRef]
18. Mifsud, D.V.; Herczku, P.; Ramachandran, R.; Sundararajan, P.; Rahul, K.K.; Kovács, S.T.S.; Sulik, B.; Juhász, Z.; Rácz, R.; Biri, S.; et al. A Systematic Mid-Infrared Spectroscopic Study of Thermally Processed H_2S Ices. *Spectrochim. Acta Part A Mol. Biomol. Spectrosc.* **2024**, *319*, 124567. [CrossRef] [PubMed]
19. Zhang, J.; Muiña, A.T.; Mifsud, D.V.; Kaňuchová, Z.; Cielinska, K.; Herczku, P.; Rahul, K.K.; Kovács, S.T.S.; Rácz, R.; Santos, J.C.; et al. A Systematic IR and VUV Spectroscopic Investigation of Ion, Electron, and Thermally Processed Ethanolamine Ice. *Mon. Not. R. Astron. Soc.* **2024**, *533*, 826–840. [CrossRef]
20. Wang, J.; Turner, A.M.; Marks, J.H.; Fortenberry, R.C.; Kaiser, R.I. Formation of Paraldehyde ($C_6H_{12}O_3$) in Interstellar Analog Ices of Acetaldehyde Exposed to Ionizing Radiation. *ChemPhysChem* **2024**, *25*, e202400837. [CrossRef]
21. McAnally, M.; Bocková, J.; Herath, A.; Turner, A.M.; Meinert, C.; Kaiser, R.I. Abiotic Formation of Alkylsulfonic Acids in Interstellar Analog Ices and Implications for Their Detection on Ryugu. *Nat. Commun.* **2024**, *15*, 4409. [CrossRef]
22. Boogert, A.C.A.; Pontoppidan, K.M.; Lahuis, F.; Jorgensen, J.K.; Augereau, J.; Blake, G.A.; Brooke, T.Y.; Brown, J.; Dullemond, C.P.; Evans, N.J., II; et al. Spitzer Space Telescope Spectroscopy of Ices toward Low-Mass Embedded Protostars. *Astrophys. J. Suppl. Ser.* **2004**, *154*, 359–362. [CrossRef]
23. Bottinelli, S.; Boogert, A.C.A.; Bouwman, J.; Beckwith, M.; van Dishoeck, E.F.; Öberg, K.I.; Pontoppidan, K.M.; Linnartz, H.; Blake, G.A.; Evans, N.J.; et al. The C2d Spitzer Spectroscopic Survey of Ices around Low-Mass Young Stellar Objects. IV. NH_3 and CH_3OH. *Astrophys. J.* **2010**, *718*, 1100–1117. [CrossRef]
24. Öberg, K.I.; Boogert, A.C.A.; Pontoppidan, K.M.; van den Broek, S.; van Dishoeck, E.F.; Bottinelli, S.; Blake, G.A.; Evans, N.J. The Spitzer Ice Legacy: Ice Evolution from Cores to Protostars. *Astrophys. J.* **2011**, *740*, 109. [CrossRef]
25. Boogert, A.C.A.; Gerakines, P.A.; Whittet, D.C.B. Observations of the Icy Universe. *Annu. Rev. Astron. Astrophys.* **2015**, *53*, 541–581. [CrossRef]
26. Terwisscha van Scheltinga, J.; Ligterink, N.F.W.; Boogert, A.C.A.; van Dishoeck, E.F.; Linnartz, H. Infrared Spectra of Complex Organic Molecules in Astronomically Relevant Ice Matrices. *Astron. Astrophys.* **2018**, *611*, A35. [CrossRef]
27. Turner, A.M.; Bergantini, A.; Abplanalp, M.J.; Zhu, C.; Góbi, S.; Sun, B.-J.; Chao, K.-H.; Chang, A.H.H.; Meinert, C.; Kaiser, R.I. An Interstellar Synthesis of Phosphorus Oxoacids. *Nat. Commun.* **2018**, *9*, 3851. [CrossRef]
28. Zhu, C.; Eckhardt, A.K.; Chandra, S.; Turner, A.M.; Schreiner, P.R.; Kaiser, R.I. Identification of a Prismatic P_3N_3 Molecule Formed from Electron Irradiated Phosphine-Nitrogen Ices. *Nat. Commun.* **2021**, *12*, 5467. [CrossRef]
29. Rosa, C.A.; Bergantini, A.; Herczku, P.; Mifsud, D.V.; Lakatos, G.; Kovács, S.T.S.; Sulik, B.; Juhász, Z.; Ioppolo, S.; Quitián-Lara, H.M.; et al. Infrared Spectral Signatures of Nucleobases in Interstellar Ices I: Purines. *Life* **2023**, *13*, 2208. [CrossRef] [PubMed]
30. Cuppen, H.M.; Linnartz, H.; Ioppolo, S. Laboratory and Computational Studies of Interstellar Ices. *Annu. Rev. Astron. Astrophys.* **2024**, *62*, 243–286. [CrossRef]
31. McClure, M.K.; Rocha, W.R.M.; Pontoppidan, K.M.; Crouzet, N.; Chu, L.E.U.; Dartois, E.; Lamberts, T.; Noble, J.A.; Pendleton, Y.J.; Perotti, G.; et al. An Ice Age JWST Inventory of Dense Molecular Cloud Ices. *Nat. Astron.* **2023**, *7*, 431–443. [CrossRef]
32. Collings, M.P.; Anderson, M.A.; Chen, R.; Dever, J.W.; Viti, S.; Williams, D.A.; McCoustra, M.R.S. A Laboratory Survey of the Thermal Desorption of Astrophysically Relevant Molecules. *Mon. Not. R. Astron. Soc.* **2004**, *354*, 1133–1140. [CrossRef]
33. Kruczkiewicz, F.; Dulieu, F.; Ivlev, A.V.; Caselli, P.; Giuliano, B.M.; Ceccarelli, C.; Theulé, P. Comprehensive Laboratory Constraints on Thermal Desorption of Interstellar Ice Analogues. *Astron. Astrophys.* **2024**, *686*, A236. [CrossRef]
34. Boogert, A.C.A.; Ehrenfreund, P. Interstellar Ices. In *Astrophysics of Dust*; Witt, A.N., Clayton, G.C., Draine, B.T., Eds.; APS Books: San Francisco, CA, USA, 2004; Volume 309, p. 547.
35. Gerakines, P.A.; Bray, J.J.; Davis, A.; Richey, C.R. The Strengths of Near-Infrared Absorption Features Relevant to Interstellar and Planetary Ices. *Astrophys. J.* **2005**, *620*, 1140–1150. [CrossRef]

36. D'Hendecourt, L.B.; Allamandola, L.J. Time Dependent Chemistry in Dense Molecular Clouds. III—Infrared Band Cross Sections of Molecules in the Solid State at 10 K. *Astron. Astrophys. Suppl. Ser.* **1986**, *64*, 453–467.
37. Kerkhof, O.; Schutte, W.A.; Ehrenfreund, P. The Infrared Band Strengths of CH_3OH, NH_3 and CH_4 in Laboratory Simulations of Astrophysical Ice Mixtures. *Astron. Astrophys.* **1999**, *346*, 990–994.
38. Draine, B.T. Interstellar Dust Grains. *Annu. Rev. Astron. Astrophys.* **2003**, *41*, 241–289. [CrossRef]
39. Brunngräber, R.; Wolf, S.; Kirchschlager, F.; Ertel, S. The Influence of Dust Grain Porosity on the Analysis of Debris Disc Observations. *Mon. Not. R. Astron. Soc.* **2017**, *464*, 4383–4389. [CrossRef]
40. Pilling, S.; Bonfim, V.S. The Influence of Molecular Vicinity (Expressed in Terms of Dielectric Constant) on the Infrared Spectra of Embedded Species in Ices and Solid Matrices. *RSC Adv.* **2020**, *10*, 5328–5338. [CrossRef]
41. Moore, M.H.; Ferrante, R.F.; James Moore, W.; Hudson, R. Infrared Spectra and Optical Constants of Nitrile Ices Relevant to Titan's Atmosphere. *Astrophys. J. Suppl. Ser.* **2010**, *191*, 96–112. [CrossRef]
42. Hudson, R.L.; Ferrante, R.F.; Moore, M.H. Infrared Spectra and Optical Constants of Astronomical Ices: I. Amorphous and Crystalline Acetylene. *Icarus* **2014**, *228*, 276–287. [CrossRef]
43. Hudson, R.L.; Gerakines, P.A.; Ferrante, R.F. IR Spectra and Properties of Solid Acetone, an Interstellar and Cometary Molecule. *Spectrochim. Acta Part A Mol. Biomol. Spectrosc.* **2018**, *193*, 33–39. [CrossRef]
44. Bonfim, V.S.; Pilling, S. The Influence of Chemical Environment on the Infrared Spectra of Embedded Molecules in Astrophysical Ices. *Proc. Int. Astron. Union* **2017**, *13*, 346–352. [CrossRef]
45. Cossi, M.; Scalmani, G.; Rega, N.; Barone, V. New Developments in the Polarizable Continuum Model for Quantum Mechanical and Classical Calculations on Molecules in Solution. *J. Chem. Phys.* **2002**, *117*, 43–54. [CrossRef]
46. Scalmani, G.; Frisch, M.J. Continuous Surface Charge Polarizable Continuum Models of Solvation. I. General Formalism. *J. Chem. Phys.* **2010**, *132*, 114110. [CrossRef] [PubMed]
47. Cancès, E.; Mennucci, B.; Tomasi, J. A New Integral Equation Formalism for the Polarizable Continuum Model: Theoretical Background and Applications to Isotropic and Anisotropic Dielectrics. *J. Chem. Phys.* **1997**, *107*, 3032–3041. [CrossRef]
48. Woon, D.E. Pathways to Glycine and Other Amino Acids in Ultraviolet-Irradiated Astrophysical Ices Determined via Quantum Chemical Modeling. *Astrophys. J.* **2002**, *571*, L177–L180. [CrossRef]
49. Park, J.-Y.; Woon, D.E. Theoretical Investigation of OCN^- Charge-Transfer Complexes in Condensed-Phase Media: Spectroscopic Properties in Amorphous Ice. *J. Phys. Chem. A* **2004**, *108*, 6589–6598. [CrossRef]
50. Woon, D.E.; Park, J. Photoionization of Benzene and Small Polycyclic Aromatic Hydrocarbons in Ultraviolet-processed Astrophysical Ices: A Computational Study. *Astrophys. J.* **2004**, *607*, 342–345. [CrossRef]
51. Pilling, S.; Baptista, L.; Boechat-Roberty, H.M.; Andrade, D.P.P. Formation Routes of Interstellar Glycine Involving Carboxylic Acids: Possible Favoritism Between Gas and Solid Phase. *Astrobiology* **2011**, *11*, 883–893. [CrossRef] [PubMed]
52. Bonfim, V.S.; Castilho, R.B.; Baptista, L.; Pilling, S. SO_3 Formation from the X-Ray Photolysis of SO_2 Astrophysical Ice Analogues: FTIR Spectroscopy and Thermodynamic Investigations. *Phys. Chem. Chem. Phys.* **2017**, *19*, 26906–26917. [CrossRef] [PubMed]
53. Woon, D.E. Benchmarking Time-Dependent Density Functional Theory for the Prediction of Electronic Absorption Spectra of Amorphous Ices for Astrochemical Applications. *Mol. Phys.* **2024**, *122*, e2254419. [CrossRef]
54. Rudberg, E.; Rubensson, E.H.; Sałek, P.; Kruchinina, A. Ergo: An Open-Source Program for Linear-Scaling Electronic Structure Calculations. *SoftwareX* **2018**, *7*, 107–111. [CrossRef]
55. Karssemeijer, L.J.; de Wijs, G.A.; Cuppen, H.M. Interactions of Adsorbed CO_2 on Water Ice at Low Temperatures. *Phys. Chem. Chem. Phys.* **2014**, *16*, 15630. [CrossRef] [PubMed]
56. Thanthiriwatte, K.S.; Duke, J.R.; Jackson, V.E.; Felmy, A.R.; Dixon, D.A. High-Level Ab Initio Predictions of the Energetics of $mCO_2 \cdot (H_2O)_n$ (n = 1–3, m = 1–12) Clusters. *J. Phys. Chem. A* **2012**, *116*, 9718–9729. [CrossRef] [PubMed]
57. Geiger, P.; Dellago, C.; Macher, M.; Franchini, C.; Kresse, G.; Bernard, J.; Stern, J.N.; Loerting, T. Proton Ordering of Cubic Ice Ic: Spectroscopy and Computer Simulations. *J. Phys. Chem. C* **2014**, *118*, 10989–10997. [CrossRef] [PubMed]
58. Drechsel-Grau, C.; Marx, D. Collective Proton Transfer in Ordinary Ice: Local Environments, Temperature Dependence and Deuteration Effects. *Phys. Chem. Chem. Phys.* **2017**, *19*, 2623–2635. [CrossRef]
59. Tanaka, H.; Okabe, I. Thermodynamic Stability of Hexagonal and Cubic Ices. *Chem. Phys. Lett.* **1996**, *259*, 593–598. [CrossRef]
60. Moore, E.B.; Molinero, V. Is It Cubic? Ice Crystallization from Deeply Supercooled Water. *Phys. Chem. Chem. Phys.* **2011**, *13*, 20008. [CrossRef] [PubMed]
61. Sandford, S.A.; Allamandola, L.J. The Physical and Infrared Spectral Properties of CO_2 in Astrophysical Ice Analogs. *Astrophys. J.* **1990**, *355*, 357. [CrossRef] [PubMed]
62. Chai, J.-D.; Head-Gordon, M. Long-Range Corrected Hybrid Density Functionals with Damped Atom–Atom Dispersion Corrections. *Phys. Chem. Chem. Phys.* **2008**, *10*, 6615. [CrossRef] [PubMed]
63. Ditchfield, R.; Hehre, W.J.; Pople, J.A. Self-Consistent Molecular-Orbital Methods. IX. An Extended Gaussian-Type Basis for Molecular-Orbital Studies of Organic Molecules. *J. Chem. Phys.* **1971**, *54*, 724–728. [CrossRef]

64. Hehre, W.J.; Ditchfield, R.; Pople, J.A. Self—Consistent Molecular Orbital Methods. XII. Further Extensions of Gaussian—Type Basis Sets for Use in Molecular Orbital Studies of Organic Molecules. *J. Chem. Phys.* **1972**, *56*, 2257–2261. [CrossRef]
65. Hariharan, P.C.; Pople, J.A. The Influence of Polarization Functions on Molecular Orbital Hydrogenation Energies. *Theor. Chim. Acta* **1973**, *28*, 213–222. [CrossRef]
66. Clark, T.; Chandrasekhar, J.; Spitznagel, G.W.; von R.Schleyer, P. Efficient Diffuse Function-Augmented Basis Sets for Anion Calculations. III. The 3-21+G Basis Set for First-Row Elements, Li-F. *J. Comput. Chem.* **1983**, *4*, 294–301. [CrossRef]
67. Frisch, M.J.; Trucks, G.W.; Schlegel, H.B.; Scuseria, G.E.; Robb, M.A.; Cheeseman, J.R.; Scalmani, G.; Barone, V.; Mennucci, B.; Petersson, G.A.; et al. *Gaussian 16, Revision C.01*; Gaussian, Inc.: Wallingford, CT, USA, 2016.
68. Ramachandran, C.N.; Ruckenstein, E. Water Clustering in the Presence of a CO_2 Molecule. *Comput. Theor. Chem.* **2011**, *966*, 84–90. [CrossRef]
69. Schiltz, L.; Escribano, B.; Muñoz Caro, G.M.; Cazaux, S.; del Burgo Olivares, C.; Carrascosa, H.; Boszhuizen, I.; González Díaz, C.; Chen, Y.-J.; Giuliano, B.M.; et al. Characterization of Carbon Dioxide on Ganymede and Europa Supported by Experiments: Effects of Temperature, Porosity, and Mixing with Water. *Astron. Astrophys.* **2024**, *688*, A155. [CrossRef]
70. Dartois, E.; D'Hendecourt, L. Search for NH_3 Ice in Cold Dust Envelopes around YSOs. *Astron. Astrophys.* **2001**, *365*, 144–156. [CrossRef]
71. Pilling, S.; Duarte, E.S.; da Silveira, E.F.; Balanzat, E.; Rothard, H.; Domaracka, A.; Boduch, P. Radiolysis of Ammonia-Containing Ices by Energetic, Heavy, and Highly Charged Ions inside Dense Astrophysical Environments. *Astron. Astrophys.* **2010**, *509*, A87. [CrossRef]
72. Pilling, S.; Duarte, E.S.; Domaracka, A.; Rothard, H.; Boduch, P.; Silveira, E.F. da Radiolysis of Astrophysical Ice Analogs by Energetic Ions: The Effect of Projectile Mass and Ice Temperature. *Phys. Chem. Chem. Phys.* **2011**, *13*, 15755. [CrossRef] [PubMed]
73. Pilling, S.; Andrade, D.P.P.; da Silveira, E.F.; Rothard, H.; Domaracka, A.; Boduch, P. Formation of Unsaturated Hydrocarbons in Interstellar Ice Analogues by Cosmic Rays. *Mon. Not. R. Astron. Soc.* **2012**, *423*, 2209–2221. [CrossRef]
74. Maté, B. Infrared Optical Constants and Band Strengths of Ices. In *Laboratory Astrophysics*; Astrophysics and Space Science Library, Volume 451; Muñoz Caro, G., Escribano, R., Eds.; Springer: Cham, Switzerland, 2018; pp. 71–86.
75. Schmitt, B.; Quirico, E.; Trotta, F.; Grundy, W.M. Optical Properties of Ices From UV to Infrared. In *Solar System Ices*; Astrophysics and Space Science Library, Volume 227; Schmitt, B., De Bergh, C., Festou, M., Eds.; Springer: Dordrecht, The Netherlands, 1998; pp. 199–240.
76. Luna, R.; Molpeceres, G.; Ortigoso, J.; Satorre, M.A.; Domingo, M.; Maté, B. Densities, Infrared Band Strengths, and Optical Constants of Solid Methanol. *Astron. Astrophys.* **2018**, *617*, A116. [CrossRef]
77. Bossa, J.-B.; Isokoski, K.; de Valois, M.S.; Linnartz, H. Thermal Collapse of Porous Interstellar Ice. *Astron. Astrophys.* **2012**, *545*, A82. [CrossRef]
78. Strazzulla, G.; Baratta, G.A.; Leto, G.; Foti, G. Ion-Beam–Induced Amorphization of Crystalline Water Ice. *Europhys. Lett.* **1992**, *18*, 517–522. [CrossRef]
79. Leto, G.; Baratta, G.A. Ly-α Photon Induced Amorphization of Ic Water Ice at 16 Kelvin. *Astron. Astrophys.* **2003**, *397*, 7–13. [CrossRef]
80. Mejía, C.; de Barros, A.L.F.; Duarte, E.S.; da Silveira, E.F.; Dartois, E.; Domaracka, A.; Rothard, H.; Boduch, P. Compaction of Porous Ices Rich in Water by Swift Heavy Ions. *Icarus* **2015**, *250*, 222–229. [CrossRef]
81. Pilling, S.; Bergantini, A. The Effect of Broadband Soft X-Rays in SO_2-Containing Ices: Implications on the Photochemistry of Ices toward Young Stellar Objects. *Astrophys. J.* **2015**, *811*, 151. [CrossRef]
82. Baragiola, R.A.; Famá, M.A.; Loeffler, M.J.; Palumbo, M.E.; Raut, U.; Shi, J.; Strazzulla, G. Gudipati, M., Castillo-Rogez, J., Eds.; Radiation Effects in Water Ice in the Outer Solar System. In *The Science of Solar System Ices*; Astrophysics and Space Science Library, Volume 356; Springer: New York, NY, USA, 2013; pp. 527–549.
83. Bouwman, J.; Ludwig, W.; Awad, Z.; Öberg, K.I.; Fuchs, G.W.; van Dishoeck, E.F.; Linnartz, H. Band Profiles and Band Strengths in Mixed H_2O:CO Ices. *Astron. Astrophys.* **2007**, *476*, 995–1003. [CrossRef]